Three-dimensional buoyant hydraulic fractures: finite volume release
Supplementary Material

Andreas Möri and Brice Lecampion

April 3, 2023

Contents

1 Approximated toughness dominated solution $\hat{\mathbf{K}}^{[V]}$

The main hypotheses of the 3-D $\widehat{K}^{[V]}$ GG (2014) solution do not differ from their constant release counterparts. Both assume a toughness-dominated 3-D buoyant fracture head with a finger-like tail far enough from the source point to feel any influence of it (e.g. large aspect ratios). The strictly hydrostatic net pressure in the head leads to a constant volume and geometry head. Due to the finite volume release, the net pressure in the tail is no longer uniform along its length. A 2-D plane-strain approach with constant pressure is still possible along the horizontal cross-section.

1.1 Toughness dominated head

This part of the fracture is strictly identical to the 3-D $\widehat{K}$ GG (2014) solution, described in section 1.1 of the Supplementary Material of Möri and Lecampion [2022].

1.2 Viscous tail

The tail only differs in its overall volume balance, which is given by

$$b \int_0^{\ell^{tail}} \bar{w}\,(z,t)\,\mathrm{d}z = V_o - V^{\mathrm{head}} \tag{1}$$

where the opening now depends on time and location. For all other details, we refer the reader to section 1.2 of the Supplementary Material of Möri and Lecampion [2022].

With these hypotheses at hand, one can obtain the similarity solutions through the usual methods (see Spence et al. [1987], Lister [1990], Spence and Turcotte [1990]) as

$$\ell^{tail}\,(t) \approx 2.60603 \frac{V_o^{2/3} \Delta\gamma^{7/9}\, t^{1/3}}{K_{Ic}^{4/9} \mu'^{1/3}} - 2.05837 \frac{K_{Ic}^{4/3} t^{1/3}}{E'^{2/3} \Delta\gamma^{1/3} \mu'^{1/3}} \approx 2.60603 \ell_{\widehat{k}}^{[V]}\,(t) - 2.05837 \frac{K_{Ic}^{4/3} t^{1/3}}{E'^{2/3} \Delta\gamma^{1/3} \mu'^{1/3}} \tag{2}$$

we substitute $\ell^{tail} = \gamma^{tail} \ell_{\widehat{k}}^{[V]}\,(t = t_s)$ to obtain

$$\gamma^{tail} \approx 2.60603 \frac{Q_o^{1/3} t^{1/3}}{V_o^{1/3}} - 2.05837 \frac{K_{Ic}^{16/9} Q_o^{1/3} t^{1/3}}{E'^{2/3} V_o \Delta\gamma^{10/9}} \tag{3}$$

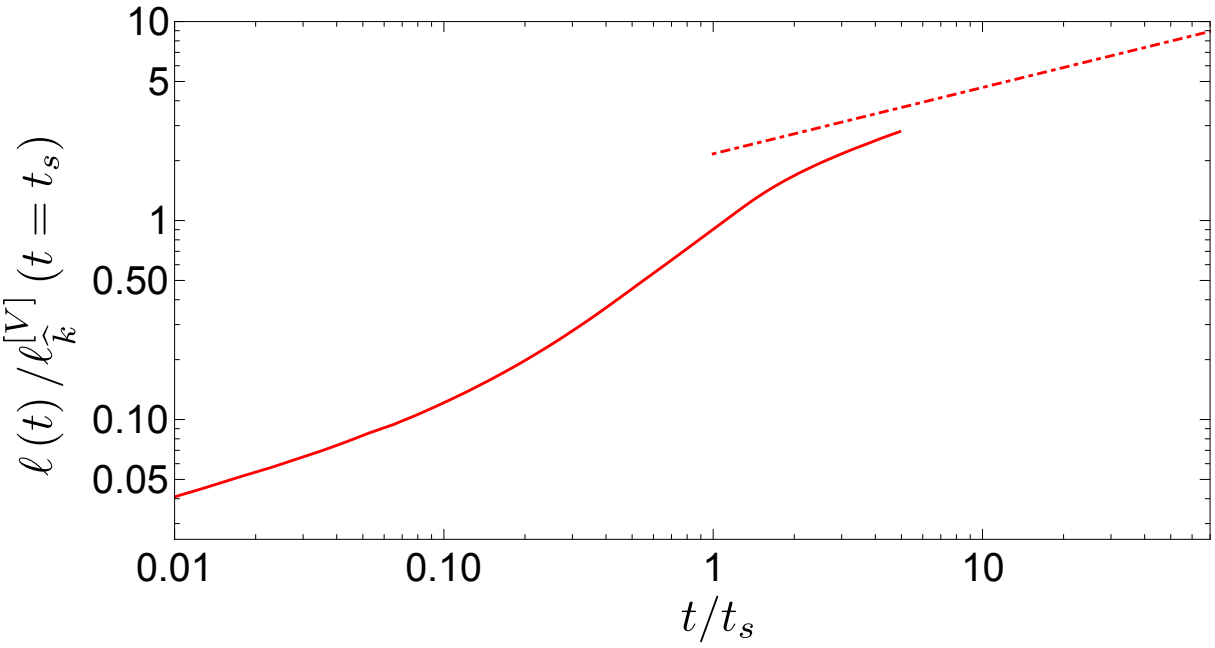

Figure 1: Height evolution of a toughness-dominated fracture together with the 3-D $\widehat{K}^{[V]}$ GG (2014) according to equation (4).

and replace $t = \tau t_s$ to obtain

$$\gamma^{tail} \approx 2.60603\tau^{1/3}\left(1 - 0.78985\frac{K_{Ic}^{16/9}}{E'^{2/3}V_o^{2/3}\Delta\gamma^{10/9}}\right) \approx 2.60603\tau^{1/3}\left(1 - 0.78985\mathcal{B}_{ks}^{-10/9}\right). \tag{4}$$

This equation shows that we will reach the tail solution within a certain percentage only. This difference, respectively the change in the pre-factor, depends on the value of the dimensionless buoyancy $\mathcal{B}_{ks}$.

$$\varepsilon\, 2.60603\tau^{1/3} = \gamma^{\text{tail}} \rightarrow \varepsilon = 1 - 0.78985\mathcal{B}_{ks}^{-10/9} \tag{5}$$

where ε is the change in the prefactor to the tail scaling one obtains for the given parameter combination. To observe the scaling predicted by the $\widehat{K}^{[V]}$ solution presented in the article (e.g. $\ell^{tail}(t) = 2.60603\ell_{\widehat{k}}^{[V]}(t)$) within an error of 5%, we would need a dimensionless buoyancy of the order of

$$\mathcal{B}_{ks}^{\varepsilon=5\%} \geq 11.9872. \tag{6}$$

When applying this to figure 4b) of the main article, we show with an orange dotted line the main trend

$$\gamma^{tail} \approx 2.60603\tau^{1/3} \tag{7}$$

and omit the details of the dependency on $\mathcal{B}_{ks}$because only one simulation (the one showing the linear trend in the continuous release case) could effectively show these details. We hence report the exact prediction for this simulation only in figure 1 and observe a minimal error to the end of the simulation of about 24%. If propagation continues, the error decreases further. For a discussion of why we do not report further ongoing simulations, we refer the reader to section 5.1.1 of the main article.

We further get the scales of the opening and pressure of their solution, which are, respectively

$$\overline{w}(t) = 0.845257\frac{V_o^{1/3}\mu'^{1/3}}{K_{Ic}^{2/9}\Delta\gamma^{1/9}t^{1/3}} = 0.845257w_{\widehat{k}}^{[V]}(t) \tag{8}$$

$$p(t) = 0.790216\frac{E'V_o^{1/3}\Delta\gamma^{5/9}\mu'^{1/3}}{K_{Ic}^{8/9}t^{1/3}} = 0.790216p_{\widehat{k}}^{[V]}(t). \tag{9}$$

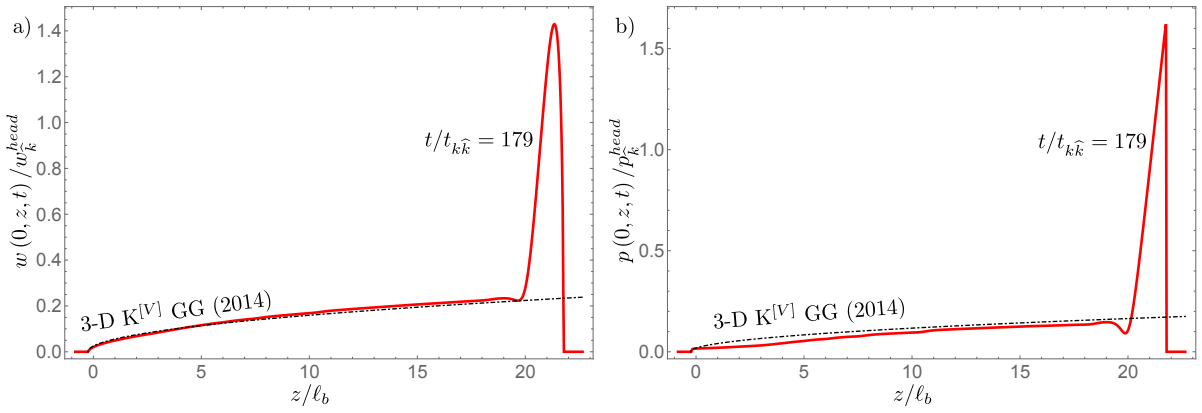

Figure 2: Opening (a) and pressure (b) along the centerline (e.g. $x = 0$) for a toughness-dominated simulation with $\mathcal{M}_{\widehat{k}} = 1$ and $\mathcal{B}_{ks} = 2$ at $t/t_{k\widehat{k}} = 179$. Black dashed-dotted lines show the tail solutions of equations (10) and (11).

More interesting to see is the evolution of the average opening and pressure with the coordinate z

$$\overline{w}(z,t) = 0.523599\frac{\mu'^{1/2}}{\Delta\gamma^{1/2}t^{1/2}}z^{1/2}. \underset{x=0}{\rightarrow} w(z,t) = \frac{2}{3}\frac{\mu'^{1/2}}{\Delta\gamma^{1/2}t^{1/2}}z^{1/2} \tag{10}$$

$$p(z,t) = 0.489504\frac{E'\Delta\gamma^{1/6}\mu'^{1/2}}{K_{Ic}^{2/3}t^{1/2}}z^{1/2}. \tag{11}$$

In figure 1, we show the opening and pressure profile at the last time step of the simulation with $\mathcal{M}_{\widehat{k}} = 1$ and $\mathcal{B}_{ks} = 2$ reported in figure 4) of the main article. One observes that the match obtained using equations (10) and (11) is very accurate.

1.3 Limit of applicability of their theory

This solution is only valid if the pressure in the tail does not allow for lateral expansion (e.g. the fracture breadth does not grow). In other terms, the pressure in the tail must at all times be $p(z,t) \leq K_{Ic}/\sqrt{0.782257\ell_b}$. As the pressure in the tail reduces, this condition verifies at a given time during fracture propagation. Garagash and Germanovich [2014] derive this limit as

$$\frac{V_o/V_*}{t/t_*} < 0.352139 \tag{12}$$

which be transformed in a stabilization time of the form

$$t_{stab} = 0.545885t_{\widehat{m}\widehat{k}}^{[V]}\mathcal{B}_{ks}^{5/12}. \tag{13}$$

The fact that lateral stabilization occurs later than the transition of the tail from viscosity- to toughness-dominated propagation (because $\mathcal{B}_{ks} \geq 1$ for buoyant fractures) explains why we have such a hard time showing simulations validating the toughness-dominated limit after being viscosity-dominated. Figure 5a) of the main article shows this problem, and we sketch the computational cost implied in section 5.1.1.

2 Self-similarity of the zero-toughness solution

We mention in section 5.2 of the main article that the evolution of a zero-toughness, finite volume, buoyant hydraulic fracture becomes nearly self-similar at a late time. This self-similarity is function of the scales presented in equation (5.6) of the main article

$$\ell_{\widehat{m}}^{[V]} = \frac{V_o^{1/2}\Delta\gamma^{1/2}t^{1/3}}{E'^{1/6}\mu'^{1/3}}, \quad b_{\widehat{m}}^{[V]} = \frac{E'^{1/4}V_o^{1/4}}{\Delta\gamma^{1/4}}$$
$$w_{\widehat{m}}^{[V]} = \frac{V_o^{1/4}\mu'^{1/3}}{E'^{1/12}\Delta\gamma^{1/4}t^{1/3}}, \quad p_{\widehat{m}}^{[V]} = \frac{E'^{2/3}\mu'^{1/3}}{t^{1/3}}. \tag{14}$$

Figure 3 shows a simulation with $\mathcal{M}_{\widehat{k}} = \mathcal{B}_{ks} = \infty$ and $\mathcal{B}_{ms} = 10^{-3}$ (e.g. transitioning from radial to buoyant in the viscosity-dominated pulse M$^{[V]}$-regime) where we report all quantities scaled by the scaling of equation (14). Note that we use a shifted z coordinate $\widehat{z}$ as to have $\widehat{z} = 0$ coinciding with the lowest point of the fracture.

The horizontal scale of the footprint is time-independent, whereas its vertical scale depends on time as $\ell^{[V]}_{\widehat{m}} \propto t^{1/3}$. One observes that after the transition, the total height of the fracture (e.g. the highest point in the scaled simulation) no longer changes. Simultaneously, fracture propagation becomes akin to the scaling, as depicted in figure 6c of the main article. Such is the case for times later than $t/t^{[V]}_{m\widehat{m}} \gtrsim 10$, even though the footprint shape is still elliptical. During ongoing propagation, the shape becomes more and more avocado-like before approaching self-similarity for $t/t^{[V]}_{m\widehat{m}} \gtrsim 800$. The resulting footprint is similar to the self-similar shape of a zero-toughness, continuous-release, buoyant hydraulic fracture (see figure 5 of Möri and Lecampion [2022]), albeit elongated. As in this continuous release case, the nearly self-similar shape occurence relates to the head volume becoming negligible compared to the total release volume. This effect is visible in figure 3b, where the head to the right becomes smaller and no longer shows significantly more cross-section volume than the adjacent parts of the tail. The detail of the head becomes negligible when observing the overall shape even though it still governs the propagation rate.

Similarly to the continuous release case, the footprint becomes flat around the centerline $x = 0$ (see figure 3a), indicating that the approximation of a 2-D plain strain fracture at the centerline might be applicable. Roper and Lister [2007] sketched such a solution in section 6 of their article and derived the fracture height (see their equation (6.7)). Interestingly, this two-dimensional evolution is equivalent to the scaling for the toughness-dominated case of equation (10) but without a prefactor

$$w^{lister}(z,t) = \frac{\mu'^{1/2}}{\Delta\gamma^{1/2} t^{1/2}} z^{1/2}. \tag{15}$$

Scaling with $\Omega = w^{lister}(z,t)/w^{[V]}_{\widehat{m}}$ and using the dimensionless coordinate $\widehat{\zeta} = \widehat{z}/\ell^{[V]}_{\widehat{m}}$ we obtain

$$\Omega\left(\widehat{\zeta}\right) = \sqrt{\widehat{\zeta}} \tag{16}$$

shown as a blue dashed line in figure 3c. The match close to the source region is astonishing and holds even if the width constraint becomes activated close to the source point. In the proximity of the propagating head, the solution seems to deviate because of 3-D effects. Nonetheless, combining the zero toughness head solution (c.f. figure 7 of Möri and Lecampion [2022]) with equation (16), could result in a complete description of zero toughness, buoyant, finite volume fractures.

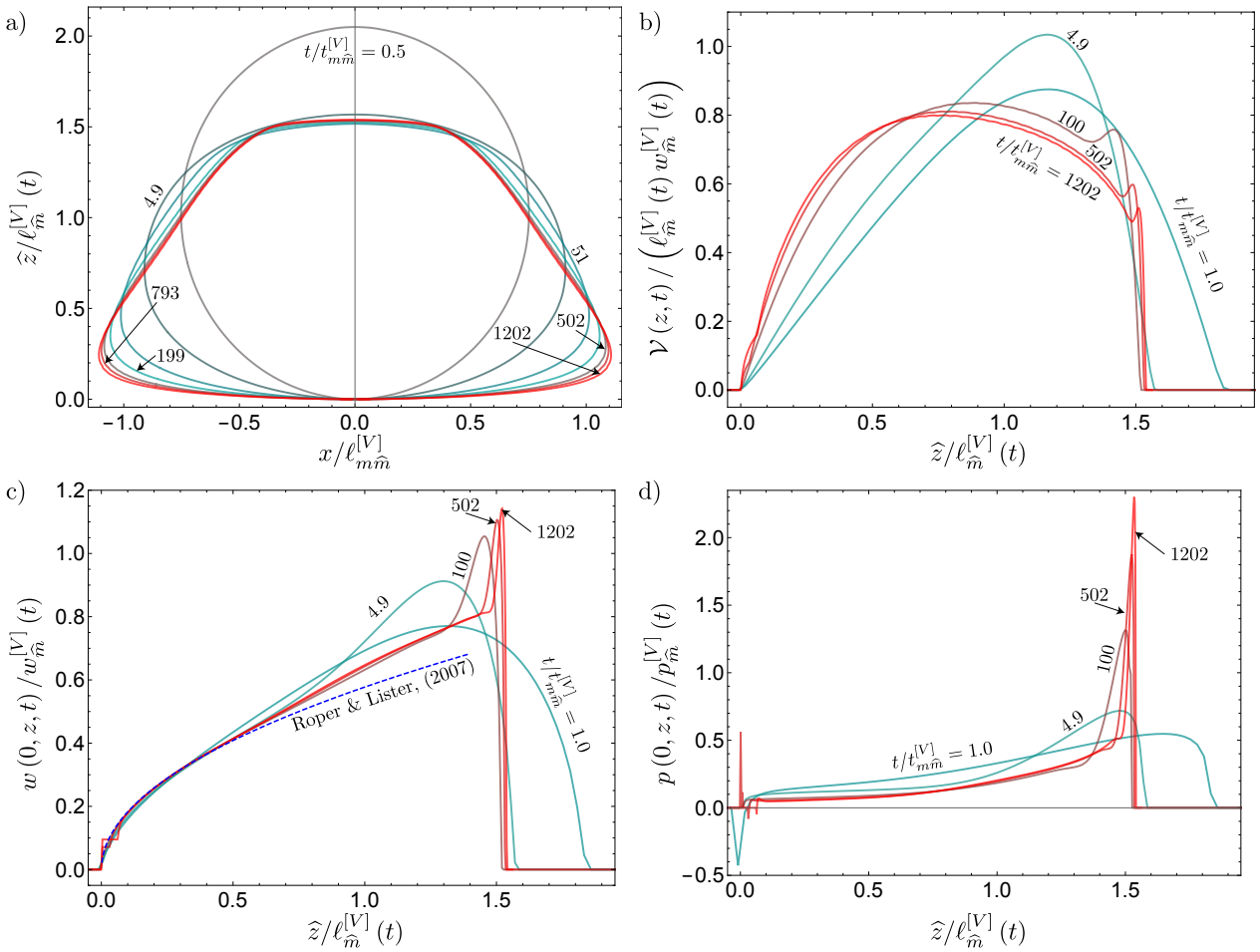

Figure 3: Footprint (a), cross-sectional volume (b), opening (c), and pressure (d) of a zero-toughness, finite volume buoyant hydraulic fracture scaled by the corresponding $\hat{\mathrm{M}}^{[V]}$-scaling (see equation (14), or equation (5.6) of the main article). The blue dashed line in c) indicates the solution presented by Roper and Lister [2007].

References

D. I. Garagash and L. N. Germanovich. Gravity driven hydraulic fracture with finite breadth. In A. Bajaj, P. Zavattieri, M. Koslowski, and T. Siegmund, editors, *Proceedings of the Society of Engineering Science 51st Annual Technical Meeting*. West Lafayette: Purdue University Libraries Scholarly Publishing Service, 1–3 October 2014.

J.R. Lister. Buoyancy-driven fluid fracture: the effects of material toughness and of low-viscosity precursors. *J. Fluid Mech.*, 210:263–280, 1990.

A. Möri and B. Lecampion. Three-dimensional buoyant hydraulic fractures: constant release from a point source. *J. Fluid Mech.*, 950:A12, 18 October 2022. doi: DOI: 10.1017/jfm.2022.800.

S. M. Roper and J. R. Lister. Buoyancy-driven crack propagation: the limit of large fracture toughness. *J. Fluid Mech.*, 580:359–380, 2007.

D. A. Spence and D. L. Turcotte. Buoyancy-driven magma fracture: A mechanism for ascent through the lithosphere and the emplacement of diamonds. *J. Geophys. Res. Solid Earth*, 95(B4):5133–5139, 1990. doi: https://doi.org/10.1029/JB095iB04p05133.

D. A. Spence, P. W. Sharp, and D. L. Turcotte. Buoyancy-driven crack propagation: a mechanism for magma migration. *J. Fluid Mech.*, 174:135–153, 1987.